Directional saturation of a strongly bimodal pore size distribution carbon interlock fabric: Measurement and multiphase flow modeling

Gabriela Gambarini, Gabriel Valdés-Alonzo, Christophe Binetruy, Sebastien Comas-Cardona, Elena Syerko, Marc Waris

Composites Part B 281 (2024) 111532

Contents lists available at ScienceDirect

Composites Part B

journal homepage: www.elsevier.com/locate/composites

Directional saturation of a strongly bimodal pore size distribution carbon interlock fabric: Measurement and multiphase flow modeling

Gabriela Gambarini [a,b], Gabriel Valdés-Alonzo [a], Christophe Binetruy [a,*], Sébastien Comas-Cardona [a], Elena Syerko [a], Marc Waris [c]

[a] Nantes Université, Ecole Centrale Nantes, CNRS, GeM, UMR 6183, F-44000, Nantes, France
[b] IRT M2P, 4 rue Augustin Fresnel, Metz, 57070, France
[c] Safran Composites, 33 avenue de la Gare, Itteville, 91760, France

ARTICLE INFO

Keywords:
Tensorial relative permeability
Unsaturation directionality
Anisotropic porous materials

ABSTRACT

This study focuses on the analysis of the directionality of saturation of materials with bimodal pore size distributions. The material studied is an anisotropic carbon interlock with highly contrasted dual-scale porosity, with heavy warp and light weft tows. Experimentally, 6 configurations are tested using injection combined with dielectric sensors to measure saturation times and unsaturated lengths. The experimental results show that this material has a high contrast in dual-scale porosity and the unsaturation is anisotropic. In parallel, a two-phase flow in porous media continuum model is developed within the OpenFOAM® toolbox of libraries to simulate the transient impregnation. The need to use a tensorial relative permeability and its alignment with the saturated permeability is analyzed by a numerical multiphase mesoscale flow model. The combined experimental and numerical analysis paves the way for a methodology to analyze the saturation of various bimodal pore size distribution materials.

1. Introduction

The family of liquid composite moulding processes is commonly used to manufacture structural composites. They are wet processes based on the principle of impregnating the fiber reinforcements, previously positioned in the cavity of a mould, by a low viscosity resin. The quality of the impregnation is measured by the percentage of pore space completely saturated by the resin. These processes can be optimized from models relating process control parameters, part geometry and material properties and behavior. Permeability is a key property of fiber reinforcement required to model flow in fiber networks, which are assimilated to porous media. The large majority of fibrous preforms used have a higher flow resistance in the thickness than in the plane. In-plane anisotropy is also common due to the directionality of the fiber arrangement in textile reinforcements. A great deal of work has been carried out to determine the permeability of fiber reinforcements, both to measure their components and to predict them using more or less sophisticated models and methods. An experimental ISO standard has recently been published to measure the permeability of anisotropic fibrous textiles [1]. In this standard, permeability can be determined by generating a steady flow in a sample completely saturated with the permeating liquid to obtain the so-called saturated (also called intrinsic, absolute or geometric) permeability. This configuration corresponds to the conditions for which Darcy permeability is defined. These data are commonly used in numerical simulation software for the manufacture of composite parts using the LCM process, although these processes necessarily involve the presence of a front that interfaces the resin with the air initially contained between the fibers. The standard also proposes a protocol for measurement under transient conditions, where the air initially present is displaced by the permeating fluid. The measured permeability is referred to as the unsaturated or effective permeability. The difference between saturated and unsaturated permeability depends mainly on the flow regime and the permeability contrast between the fiber tows and the gaps between them (it is assumed here that the scale is large enough to define the concept of permeability for the pore network between the fiber tows). Breard et al. [2] showed that the permeability can be related to the dual-scale porosity structure, and that a more detailed description of the impregnation can be made by introducing the notion of saturation and expressing the permeability as a function of it.

In the steady flow regime, wetting effects are negligible compared to viscous effects, while in the transient regime, wetting forces contribute to fiber tow impregnation. These two regimes are usually compared in terms of capillary number. When the porous medium is weakly to

* Corresponding author.
E-mail address: christophe.binetruy@ec-nantes.fr (C. Binetruy).

https://doi.org/10.1016/j.compositesb.2024.111532
Received 23 October 2023; Received in revised form 21 April 2024; Accepted 1 May 2024
Available online 7 May 2024

moderately heterogeneous, these two types of permeability are relatively similar. This means that a measurement performed in a saturated sample can be used as an input to simulate the LCM process. In practice, this is often achieved by simulating preform impregnation at the scale of the medium using a continuum modeling approach. However, there are many situations where preforms are highly heterogeneous. For example, the presence of draining high-permeability reinforcements in the core of a thick preform in low-pressure LCM processes leads to very pronounced transient phenomena characterized by planar and out-of-plane flows in the flow front zone. This mechanism becomes more pronounced the thicker the preform, the lower the through-thickness permeabilities, the greater the planar permeability variations, and the larger the stacking angles between layers [3]. It has been shown in [3] that the unsaturated permeability asymptotically tends to the saturated one and the difference between the two permeabilities can be very significant. This problem is characterized by internal lengths that make measuring permeability challenging. This high level of heterogeneity can also exist at the scale of the textile reinforcement, as in the case of 3D fabrics.

The use of new 3D woven carbon fabrics in aeronautical composite parts has gained significant attention in recent years. These pioneering fabrics offer a number of advantages over their conventional 2D counterparts, including improved inter-laminar shear strength and a reduced risk of delamination, all while contributing to weight reduction, a key objective in aerospace design.

While numerous studies have investigated the mechanical properties and impregnation of traditional 2D fabrics, the same level of attention has not been given to the comprehensive characterization of 3D fiber reinforcements. Umer et al. [4] and Endruweit et al. [5] characterized the unsaturated in-plane and transverse permeability of different interlock geometries using radial flow experiments, based on the measurement of the flow front position as a function of time. The ratio between the unsaturated permeability and the saturated intrinsic permeability can introduce significant errors in the analysis of the filling process.

In [6] Michaud reviewed approaches used to model unsaturated flow in dual-scale porosity fabrics. A first group of macroscopic methods add to fully saturated flow models a source term representing the saturation rate for tow infiltration. A more accurate approach is to numerically solve the two-scale flow in a representative volume element that captures the geometric characteristics of the porous material. This method uses the computational fluid dynamics approach to describe the interaction of flow at both scales. Finally, the third approach is a continuum mechanics approach widely used in the field of natural porous media, known as the multiphase flow approach. This method uses the ratio of effective to intrinsic permeability, known as relative permeability, to capture the delayed impregnation of the pore space and model immiscible fluid flow through porous materials. While the permeability of a textile fabric is almost universally modeled as anisotropic, the relative permeability is consistently modeled as a scalar function of saturation in composite process modeling. Although [7] pointed out that the concept of relative permeability used in unsaturated flow should be limited to isotropic media and not extended to anisotropic ones, it was later shown that the directional dependence of saturation and relative permeability is due to the heterogeneity of the porous medium, the direction of flow, and the dominant forces in the interaction between capillary, viscous, and gravitational forces [8,9].

The open complex 3D architecture, which introduces some directionality, combined with the densely packed tows (due to their twisting) used in the manufacturing of these interlock fabrics pose unique challenges in terms of experimental characterization of the transient flow within them due to the strongly bimodal pore size distribution. Industrially, it was reported that the delay of the tow impregnation is much bigger than that observed for conventional fabric reinforcements, and therefore it requires a substantial overfeeding that increases processing time and resin waste. In light of the above on the directional relative permeability concept, it also raises the question of the permeability input data to be generated for the continuum modeling of its transient impregnation.

To the best of our knowledge, this work is one of the first to address the question of the directionality of the relative permeability in the multiphase approach. The questions of the emergence of tensorial relative permeability and its alignment with saturated permeability are raised in this study.

The target of this work is to improve understanding of impregnation phenomena in a fabric characterized by a very high level of contrast and directionality of local properties in dual-scale porosity materials. The two objectives are divided as below:

1. provide experimental evidences of the directionality of the unsaturated lengths and saturation times,
2. propose a saturation modeling and a multiphase flow numerical approach that encompass directionality of saturation kinetics. The emergence of tensorial relative permeability is discussed in the context of multiphase flow up-scaling.

The proposed methodology is intended to provide a blueprint for experimental and computational analysis that can be adapted to various textile preforms with strongly bimodal pore size distributions.

The article is organized as follows. First in Section 2, the definitions and the methods used in the paper are detailed for the experimental measurements, modeling and numerical approach. Then a description of the materials of the study and the experimental and numerical test configurations are described in Section 3. In Section 4, the experimental and numerical results are given. Finally a discussion and the conclusion close the study.

2. Methods

2.1. Definition and experimental measurements of saturation

During the liquid flow in a porous material such as a fabric, impregnation occurs at the microscale, but it can be described in a macroscopic sense using permeability. The following definitions of permeability are given and used in the article:

- The saturated (intrinsic) permeability tensor $\boldsymbol{K}_{sat}$ is the permeability of a porous medium saturated by one fluid. It only depends on the geometrical pore space of the material.
- The effective permeability tensor $\boldsymbol{K}(S)$, with respect to the liquid phase l, is the permeability of a porous medium as experienced by that liquid. It includes the interfacial and wetting properties. It is sometimes called unsaturated permeability.
- The relative permeability is the ratio of the effective to the saturated permeability. It is usually a scalar $k_{r,l}$ for isotropic materials, but in more general cases it can be a tensor. In the latter case it is written as $\boldsymbol{k}_{r,l} = \boldsymbol{K}(S) \cdot \boldsymbol{K}_{sat}^{-1}$.

The saturation of a material is defined as the ratio between the volume of fluid V_{fluid} and the pore space of the total volume V_{total} within a volume of interest, giving an idea of the amount of fluid in that volume. Given a porosity ϕ, the saturation S can be defined as in Eq. (1). With that definition, the saturation values are continuous and ranging from 0 (dry) to 1 (fully saturated).

$$S = \frac{V_{fluid}}{\phi V_{total}} \tag{1}$$

Michaud [6] reviewed different experimental techniques used to measure the time-dependent saturation profile during the impregnation of fabrics. For translucent ones, such as glass fiber reinforcements, Lebel et al. [10] used visible light transmission to measure real-time impregnation and void content. Direct image analysis has also been used when flow visualization is possible [11,12]. For carbon fiber materials, direct optical monitoring of the flow is not possible due to its opaqueness.

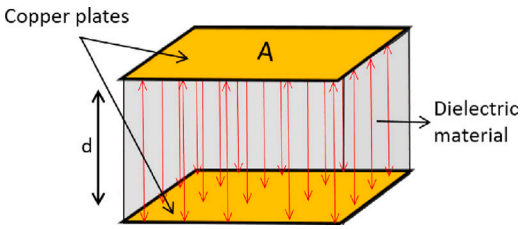

Fig. 1. Parallel plate dielectric sensor with plate surface A and distance d between plates.

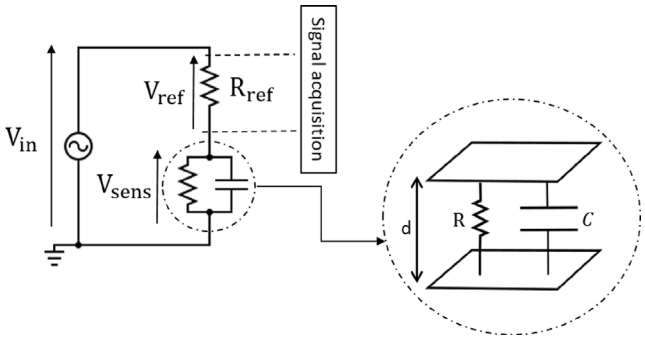

Fig. 2. Schematic of a dielectric sensor inserted in the electric circuit.

Because of this, other techniques have been investigated. Recently, Teixidó [13] has used an in-situ X-ray phase contrast technique to observe flow through both translucent and non-translucent preforms such as carbon fiber ones. Labat et al. [14] and Laurent et al. [15] used a conductivity sensor to blindly measure the saturation of the porous media using the difference in electrical conductivity between liquid air and fibers. Other authors such as Carlone et al. [16,17], Guéroult et al. [18], Hegg et al. [19], Laurent et al. [15], Pouchias et al. [20], Skordos et al. [21], Tifkitsis et al. [22], Yenilmez et al. [23] studied the change in capacitance due to the change of dielectric properties during the impregnation of a fabric. They proposed adapted and optimized setups and recommendations to extract saturation during injections.

2.2. Dielectric measurements

Hereafter is a summarized description of the dielectric sensing technique used to measure saturation. The readers can refer to [15–23] for more details and recommendations of the measurement technique. The dielectric sensor is a capacitor made of two parallel metallic plates (e.g., copper). The capacitance C (Eq. (2)) is the amount of charge the capacitor can hold and depends on the area A of the plates, the distance d between the plates, the relative permittivity ε_r of the dielectric material between the plates and the permittivity ε_0 of the vacuum (see Fig. 1).

$$C = \varepsilon_0 \varepsilon_r \frac{A}{d} \tag{2}$$

The dielectric material between the metallic plates initially consists of air and fibers (e.g., carbon) prior to injection. During impregnation, the air is replaced by a liquid until no air remains. Due to the higher relative permittivity of the fluid compared to the air, the capacitance of the sensor will increase during impregnation until the sensor is fully saturated.

An AC source powers the sensor, the latter is also connected in series with a known reference resistor R_{ref} as shown in Fig. 2. When the capacitance changes in the sensor, so do its impedance and voltage. The impedance Z_s in the sensor volume is calculated measuring the voltage V_{ref} across the known reference resistor R_{ref} using Ohm's law [15]:

$$Z_s = R_{ref} \times \frac{(V_{in} - V_{ref})}{V_{\text{ref}}} \tag{3}$$

If the impedance is known for the dry fabric (Z_{dry}) and for the fully saturated case (Z_{sat}), the saturation S can then be calculated at any time t from the measured impedance of the impregnating sample Z_s using Eq. (4) [15,22].

$$S = \frac{1/Z_s - 1/Z_{dry}}{1/Z_{sat} - 1/Z_{dry}} \tag{4}$$

2.3. Numerical saturation

The unsaturation can be considered as a continuous field, and although dielectric sensors can provide a quantitative analysis of the total fluid volume within the sensing zone, a comprehensive understanding of the various mechanisms involved in fabric impregnation, including void formation, transport and entrapment, cannot be obtained experimentally. Furthermore, the question of the origin of the tensorial relative permeability and its alignment with the saturated permeability cannot be only investigated by an experimental approach since the measurements cannot distinguish the warp and weft saturation kinetics separately.

A numerical analysis is proposed to first support the conclusions presented in the experimental part of this study and to extend the analysis to address the question of continuum modeling of the transient impregnation of textile preforms with strongly bimodal pore size distributions.

It is expected that simulations of an interlock fabric with similar properties will give results of the same order as those already observed. The analysis can be extended to other parameters at the mesoscopic scale that could not be analyzed with the experimental technique used.

At the mesoscale, a model of injection has been implemented in OpenFOAM [24], taking into account the dual-scale architecture of the fabric. It uses the Finite Volumes Method (FVM) [25] to solve the equations, which is a method that discretizes the space in volumes, as opposed to the Finite Elements Method (FEM), which works with elements. This means that the equations are solved inside a volume rather than at nodes, which is useful in fluid dynamics as it simplifies the calculation of flows and transport. OpenFOAM is not a solver in itself, but rather a collection of solvers for different purposes. One of the solvers provided, called compressibleInterFoam, is used to simulate two-phase flows in a domain. This solver is designed to account for compressibility effects, simulating the effects of air bubbles transport and counter pressure during the injection process. This solver has been modified to account for the anisotropy of the fiber tows.

For the impregnation analysis the simulation is done at the mesoscale level of the fabric. The model solves the Navier–Stokes equations using a Volume of Fluids (VoF) approach [26], where a single set of equations can be used to represent the entire mixture, so that the flow in a solid free region (inter-tow gaps) and inside the porous fiber tows are solved simultaneously [27]. The two-phase micro-continuum approach relies on single-field variables, i.e. unique fluid pressure and velocity fields that are defined throughout the entire grid regardless of the nature of the phases occupying the cells. The single-field pressure p and velocity $\boldsymbol{U}$ are defined as weighted sums of the pressure and velocity in each fluid phase:

$$p = \alpha_l p_l + \alpha_g p_g, \tag{5}$$

$$\boldsymbol{U} = \phi(\alpha_l \boldsymbol{U}_l + \alpha_g \boldsymbol{U}_g) \tag{6}$$

where α_i is the volume fraction and $i = l, g$ denote the liquid and gas phases respectively. The liquid volume fraction is analogous to the saturation S measured in the experimental setting, and ϕ represents the porosity of the volume in the same manner. The simulation is

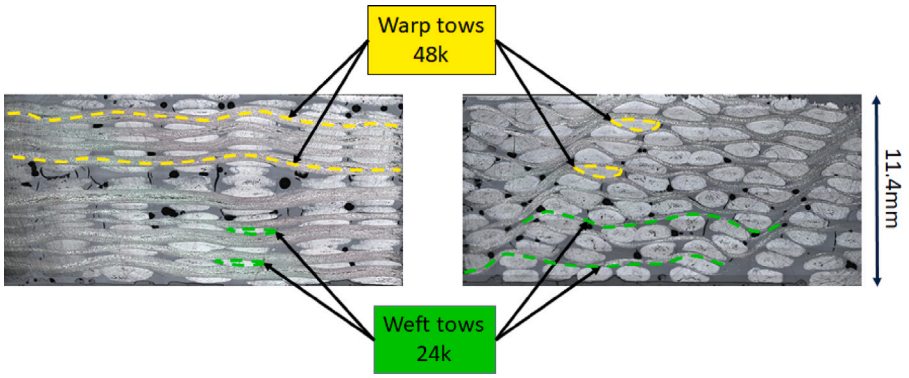

Fig. 3. Full cross-sections along the warp direction (left) and weft direction (right) of the interlock fabric of the study at $V_f = 55\%$.

performed by solving the following set of equations, respectively conservation of mass, conservation of momentum and phase transport [28,29]:

$$\frac{\partial \rho}{\partial t} + \nabla(\rho \boldsymbol{U}) = 0, \tag{7}$$

$$\frac{\partial \rho \boldsymbol{U}}{\partial t} + \nabla(\rho \boldsymbol{U}\boldsymbol{U}) = -\nabla p + \nabla(\mu \nabla \boldsymbol{U}) + S_U, \tag{8}$$

$$\frac{\partial \alpha}{\partial t} + \nabla\big(\alpha_l(\boldsymbol{U})\big) + \nabla(\alpha_g \alpha_l \boldsymbol{U}_r) = 0, \tag{9}$$

where ρ is the weighted single-field density (defined similarly to Eq. (5)), μ is the viscosity, $\boldsymbol{U}_r$ is the relative velocity between the phases, and S_U is a source term representing the volume-averaged viscous stress and the total drag force. Since they represent the fraction of each phase, it is mandatory that $\alpha_l + \alpha_g = 1$.

3. Study case

3.1. Fibrous material of the study: carbon interlock

The fabric of this study is a layer-to-layer carbon interlock produced by Safran Composites. It is composed of 16 plies and has an areal weight of 11.184 kg/m^2. Fig. 3 shows the full cross-sections along the warp and the weft directions of a polymerized sample with a fiber volume fraction $V_f = 55\%$. The anisotropy of the interlock comes from its high warp to weft weight ratio (64.4%w in the warp direction and 35.6%w in the weft direction). Moreover, the warp tows (48k) are twisted and heavier than the weft tows (24k). The interlock specimens are 240 mm × 80 mm in-plane and 20 mm-thick prior to any compaction.

Prior to the transient saturation analysis, the saturated permeability of the interlock in the warp and weft directions was measured using the continuous unidirectional compression method [30] for $40\% < V_f < 65\%$. The results given in Fig. 4 show the usual decay of saturated permeability with respect to V_f. It has also been verified, using central injections, that the in-plane principal permeability directions are superposed with the warp and weft directions. It is interesting to note that the decay in permeability along the weft direction is less than that along the warp direction. This is another indication of fluid flow anisotropy of the material at the mesoscale. As V_f increases, the tortuosity seems to evolve differently along the warp and weft directions since the decay is not identical in both directions. Moreover, the overall saturated permeability, even for $V_f > 60\%$ remains quite high for carbon fibrous materials. This emphasizes the fact that the twisted warp tows are dense (to allow high V_f) and that the inter-tow space remains (to allow not too low permeability). These first results let foresee a material that exhibits high dual-scale contrast and directionality, that will be confirmed in the Sections 4.1 and 4.2.

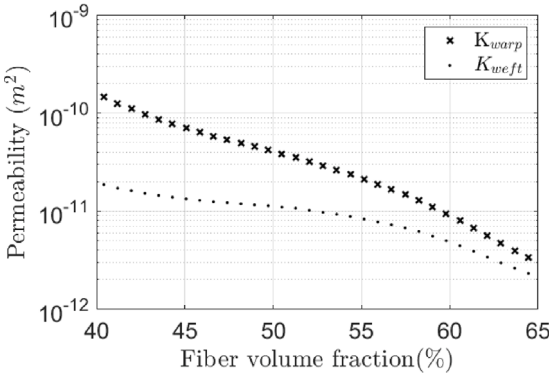

Fig. 4. Saturated permeability in the warp and weft directions.

3.2. Saturation experimental setup and sample configurations

To measure the saturation of interlock samples at different fiber volume fractions, the experimental setup must meet certain specifications. First, it should be capable of generating a high compaction stress, typically in the order of tens of bar, in order to reach the targeted fiber volume fractions. For this, a mold will be positioned between the stiff steel platens of a UTM (universal testing machine, Shimadzu AGX-V with a capacity of 100 kN). Secondly, the experimental setup should be insulated from the metallic platens of the UTM. To meet this requirement, the mold is made of PMMA polymer. Finally, the setup should allow the use of dielectric sensors with an electrically conductive interlock. A dielectric sensor consists of 2 copper plates of area 40 mm × 40 mm and facing each other with respect to the interlock thickness. The copper plates are 0.1 mm thick and are inserted in 0.1 mm grooves machined in the mold. The electrical insulation from the interlock is realized while inserting a 0.05 mm-thick polyamide film between the interlock and the sensor copper plate.

As depicted in Fig. 5, two sensors are respectively positioned at 30 mm and 170 mm from the edge and inlet of specimen. The sensors are centered with respect to the sample width, 20 mm from the interlock side edges.

A total of 6 sample configurations were carried out. Each sample was compressed to a desired fiber volume fraction V_f. The injected liquid is a blend of glycerol (Technical glycerol from VWR Chemicals) and water (water content of 14%w). The blend has a dynamic viscosity $\mu = 0.17$ Pa s at room temperature. The injections are carried out at a pressure $P_{inj} = 0.2$ bar below the atmospheric pressure, generated by a vacuum pump. The parameters of the tested configurations are summarized in Table 1.

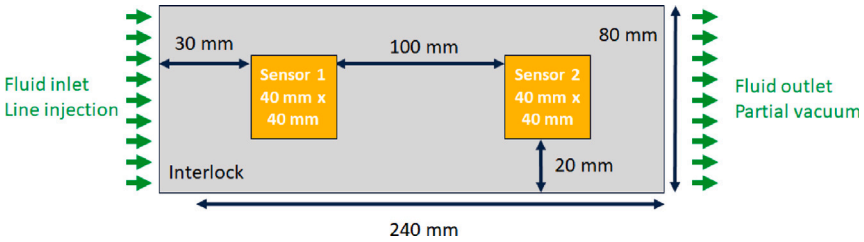

Fig. 5. Schematic top view of the dielectric sensor size and positions with respect to the interlock sample.

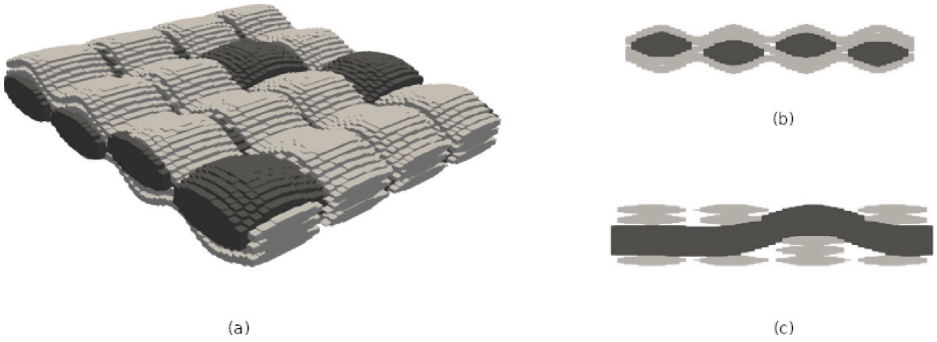

Fig. 6. (a) Geometry used to represent the unit cell of the fabric warp tows are dark gray and weft tows are light gray. (b) Slice along the weft tows. (c) Slice along the warp tows.

Table 1
List of sample configurations and test parameters (μ is the liquid viscosity and P_{inj} the injection pressure).

Dir.	V_f (%)	h (mm)	μ (Pa s)	P_{inj} (bar)
Warp	50	12.5	0.17	0.2
	55	11.4		
	62	10		
Weft	50	12.5	0.17	0.2
	55	11.4		
	62	10		

Table 2
Average geometric parameters for defining the model fabric shown in Fig. 3.

	Width (mm)	Height (mm)	Spacing (mm)
Warp	2.3	0.9	2.6
Weft	2.1	0.3	2.4

Table 3
Input parameters for flow simulation.

Input parameter	Value
$K_{tow\ \parallel}$	$1.035 \cdot 10^{-13}$ m^2
$K_{tow\ \perp}$	$2.183 \cdot 10^{-14}$ m^2
$V_{f\ tow}$	65%
μ_{fluid}	0.17 Pa s
μ_{air}	$1.983 \cdot 10^{-5}$ Pa s

3.3. Digital geometry

There are two ways to create a digital material that represents the geometry of the interlock reinforcement: high-resolution micro-computed tomography (micro-CT) imaging or using a 3D textile modeler. Regarding the lower limit of voxel size that can be acquired to capture small gaps between fiber tows while maintaining a sufficiently large field of view for 3D interlock fabric, the second approach was adopted in this study.

The geometry used to represent the interlock numerically was created using TexGen [31]. The mesh is defined as a unit cell that is infinitely repeated in three dimensions to create a full domain with a desired shape. The unit cell has been defined to closely mimic the interlock geometry and is defined as follows: thinner weft parallel tows are modeled and weaved together with thicker warp tows. The weft tows are stacked in groups of three, with the warp tows interlaced between them. This can be observed in Fig. 6, which is a qualitative approximation of what is observed in Fig. 3.

The parameters associated with the fabric are listed in Table 2. For the model to be generated, the dimensions of each tow, the distance between them (measured from the center of two consecutive tows), and the position of each tow with respect to the others is provided. It is known from the properties of the fabric that the weft tows have half the filament count of warp tows, so this information is used together with high-resolution micro-CT images to estimate these values.

The model generated with these properties has a target volume fraction of 50%, which varies slightly depending on the size of the mesh elements. All saturated permeability values used in the following calculations are based on this volume fraction value.

3.4. Simulation

The input parameters that define the material properties for the simulation are outlined in the Table 3.

In this table, μ_{fluid} is the liquid viscosity measured during the experiments, μ_{air} is a viscosity value chosen for the air, $V_{f\ tow}$ is the fiber volume fraction of the tow, and both $K_{tow\ \parallel}$ and $K_{tow\ \perp}$ are the components of the permeability tensor of the tow, the parallel one being the one taken in the axial direction of the tow, calculated from the Gebart's model [32].

In the simulation, the value of the volume fraction is used to define the porosity ϕ seen in Eq. (6). In this sense, the porosity of the tows is defined as $1 - V_{ftow}$, i.e. 0.35, while the porosity of the voids between the tows is defined as 1.

For the boundary conditions, values for pressure, saturation, and velocity must be defined for the inlet. For the outlet, only the pressure needs to be set to create a pressure drop that drives the flow from one end to the other. In the examples shown here, the pressure gradient is set to 0.2 bar to replicate the experimental conditions in sensor S1, while ensuring that the flow generated is at a low Reynolds number and

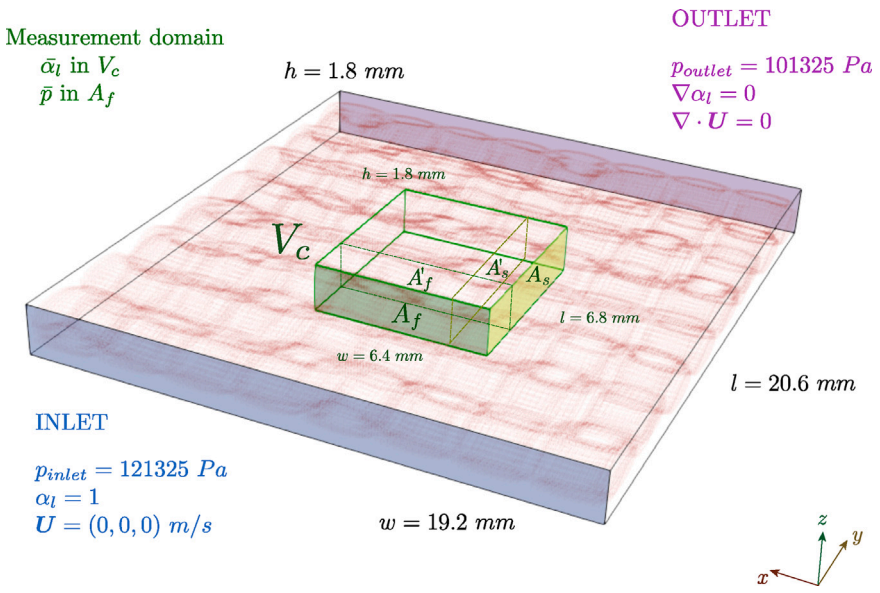

Fig. 7. Schematics of the computational domain and the applied boundary conditions. The warp is in the y direction.

Table 4
Boundary conditions applied in the numerical simulations.

Quantity	Inlet	Outlet	Walls
p (Pa)	121 325	101 325	$\nabla p = 0$
α_l	1.00	$\nabla\alpha_l = 0$	$\nabla\alpha_l = 0$
$\boldsymbol{U}$ (m/s)	**0**	$\nabla\boldsymbol{U} = 0$	$\nabla\boldsymbol{U} = 0$

dominated by viscous effects. For the remaining walls of the domain, the gradient of all properties is set to zero, meaning that there will be no flow of any quantity through these walls. All this is summarized in Table 4.

Finally, the initial state of the domain must also be described. This is done by assuming that the domain is initially unsaturated, i.e. $\alpha_l = 0$ everywhere. Also, since there is no flow, the velocity field is set to zero everywhere, and the initial pressure is just the atmospheric pressure already set at the outlet.

When analyzing the simulation, special care must be taken at the edges of the domain. Since the goal is to find results in a generic unit cell, the ideal situation would be to study an area of the domain that is far from the edges, which do not allow any flow through them. For this reason, for each simulation performed, a domain consisting of 4 unit cells is defined, with a central volume (V_c) defined as the domain of interest in Fig. 7, where measurements are taken to represent the sensor. This extension of the domain allows to push the boundary effects far away from the analyzed domain, while maintaining a representative area that can be used to extrapolate the results. In these simulations, the saturation and pressure values are computed and averaged over the entire central volume and the face of the domain, respectively. A schematic of the simulation domain with the applied boundary conditions is shown in Fig. 7, where the warp is aligned in the y-direction.

4. Results

4.1. Experimental: saturation time

The objective of this section is to prove that the interlock material exhibits high contrast in dual-scale porosity. An example of the dielectric sensor response for the injection of the interlock at $V_f = 0.55\%$ in the weft direction is given in Fig. 8. The sensors follow the expected trends. A first sharp increase due to the intertow saturation is followed

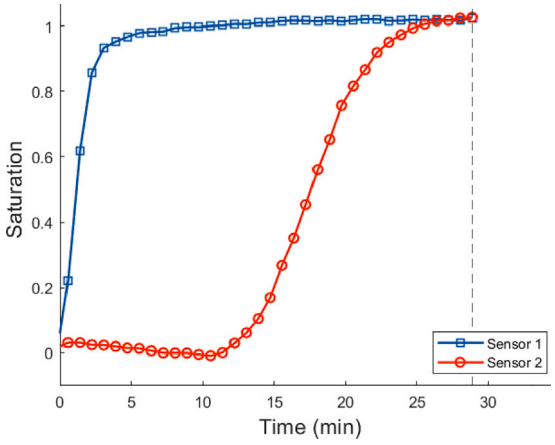

Fig. 8. Example of sensor response for the configuration of injection in the weft direction at a fiber volume fraction of 62% with an injection pressure of 0.2 bar and liquid viscosity of 0.17 Pa s.

by a slower increase as the intratows saturate. The t_{fill} is the time to fully saturate the sensing zone and it is the difference between the time of full saturation $t_{saturation}$ and the time of flow front arrival $t_{arrival}$ as shown in Fig. 9. The thresholds used to determine those times are obviously influencing the results. For the arrival time, an increase of 2% of the saturation will be the trigger. For the saturation time, a saturation of 98% will be the trigger. Other values of thresholds would modify the respective times, but the overall trends would not be affected qualitatively.

Fig. 10 shows experimental times of full saturation. As comparison, the theoretical single-scale filling time t^{sc}_{fill} is given by Eq. (11) using Darcy's law and the saturated permeability of the fabric ($\boldsymbol{K}_{sat}$).

$$\boldsymbol{K}_{sat} = \begin{bmatrix} K_{warp} & 0 \\ 0 & K_{weft} \end{bmatrix} \tag{10}$$

$$t^{sc}_{fill} = \frac{(1 - V_f)\mu}{2K_i P_{inj}} \left(L^2_{end} - L^2_{start}\right) \tag{11}$$

where L_{end} and L_{start} are respectively the flow length until the ending and starting edges of the sensor and K_i is either K_{warp} or K_{weft} relative to the tested configuration. The difference between t_{fill} and

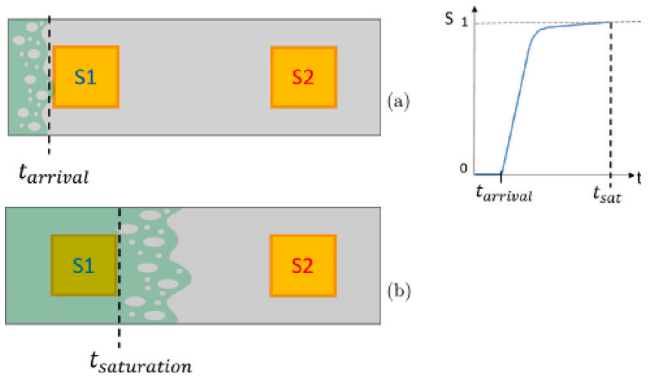

Fig. 9. Time of flow front arrival $t_{arrival}$ (a) and time of full saturation $t_{saturation}$ of the sensing area (b).

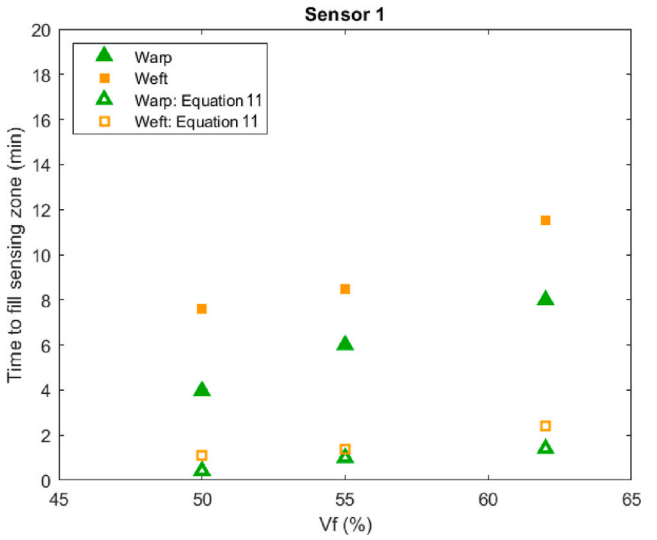

Fig. 10. Comparison between the experimental time to full impregnation t^{sc}_{fill} measured with the dielectric sensor and the theoretical single scale filling time with Eq. (11).

t^{sc}_{fill} illustrates the influence of void formation and transport on the impregnation time of the interlock due to its dual-scale strength. This difference was observed during all 6 configuration tests and bleeding time was needed in order to properly saturate the interlock.

It can be observed in Fig. 10 that the impregnation time is longer for the tests injected in the weft direction compared to those on the warp direction, which is consistent with the anisotropy of the fabric and $K_{warp} > K_{weft}$. The filling time of the interlock, is 6 times greater than the theoretical single scale filling time predicted by Eq. (11). To conclude this section, from these results, we can confirm that the interlock has a well separated and high dual-scale porosity.

4.2. Experimental: unsaturated length

The objective of this section is to show that the interlock exhibits directionality in its saturation. To do so, the test configurations have been further analyzed following the procedure proposed by Labat [33] and Gueroult [18] in order to extract the unsaturated lengths at the sensors' location. For injection at constant pressure as done in this study, at a given location in space, the liquid pressure and liquid pressure gradient is constant. Therefore unsaturation lengths can be compared for all test configurations for a given pressure and a given pressure gradient surrounding the tows in the dielectric sensor volume. As depicted in Fig. 11 the interlock exhibits quite large unsaturated lengths especially

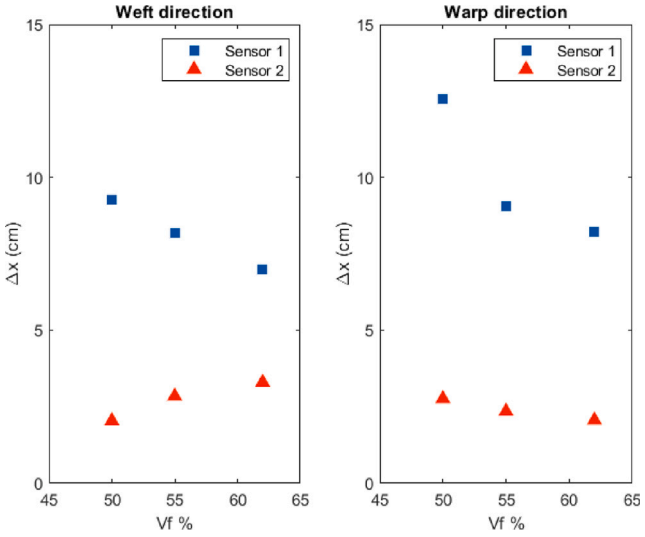

Fig. 11. Unsaturated lengths measured with the dielectric sensor for the 6 test configurations.

for the sensor 1 close to the inlet. For most usual woven fabrics used in composite manufacturing the unsaturated lengths are in the order of millimeters to a centimeter (e.g., as in [11]) compared to up to 9 cm in the interlock of the study. The measured unsaturated lengths depends on the fiber volume fraction (which modifies the dual scale strength) and depends as well on the direction of flow. For the interlock, the unsaturated length is greater in the warp direction than in the weft one. At the sensor 2 position, the differences are less pronounced, but still visible.

4.3. Simulation: saturation

A simulation of the interlock fabric with flow in the weft direction (perpendicular to the binding tows) is performed using the parameters mentioned in Section 3.4. The size of the elements is 0.2 mm × 0.2 mm × 0.033 mm, which corresponds to 21,228,480 nodes and 1,432,617 elements.

Fig. 12 shows how the resin flows through the central volume in cross sections A_f and A_s (defined in Fig. 7), which are along the warp and weft directions. The solution of the simulation shows in detail how the resin moves towards the outlet and how bubbles are formed as a result of the radial flow in the fiber tows. It is worth noting that flowing bubbles are also included in the calculation of transient saturation. It can be seen in the cross sections that even after 100 s of simulation time there are still unsaturated cells in the model, something that cannot be easily observed during the experiments. Since the visualization of the cross section shows the slice of a tow, it can be seen in detail how in section A_s it takes a very long time to impregnate the inside of the fiber tow, as opposed to the surrounding areas.

Fig. 13 shows how the resin flows through cross sections A'_f and A'_s parallel to the previous sections. In here there is a clean cut of the tows in the cross sections, so these images give a better idea of the path that the resin takes while flowing in the central volume V_c, since the intertow space is much more permeable than the fibers. Since the visualization shows an zone that is more open, the bubble entrapment is not as visible as the previous figure.

It can also be seen in Fig. 14 the streamlines showing the flow of the resin at $t = 0.025$ s in the volume V_c, also defined in Fig. 7. The streamlines are obtained from the velocity field, but their coloration depends on the values of the saturation field around them (from red being fully saturated to blue being unsaturated). Here, the same phenomena are visualized in three dimensions, and it is easier to see

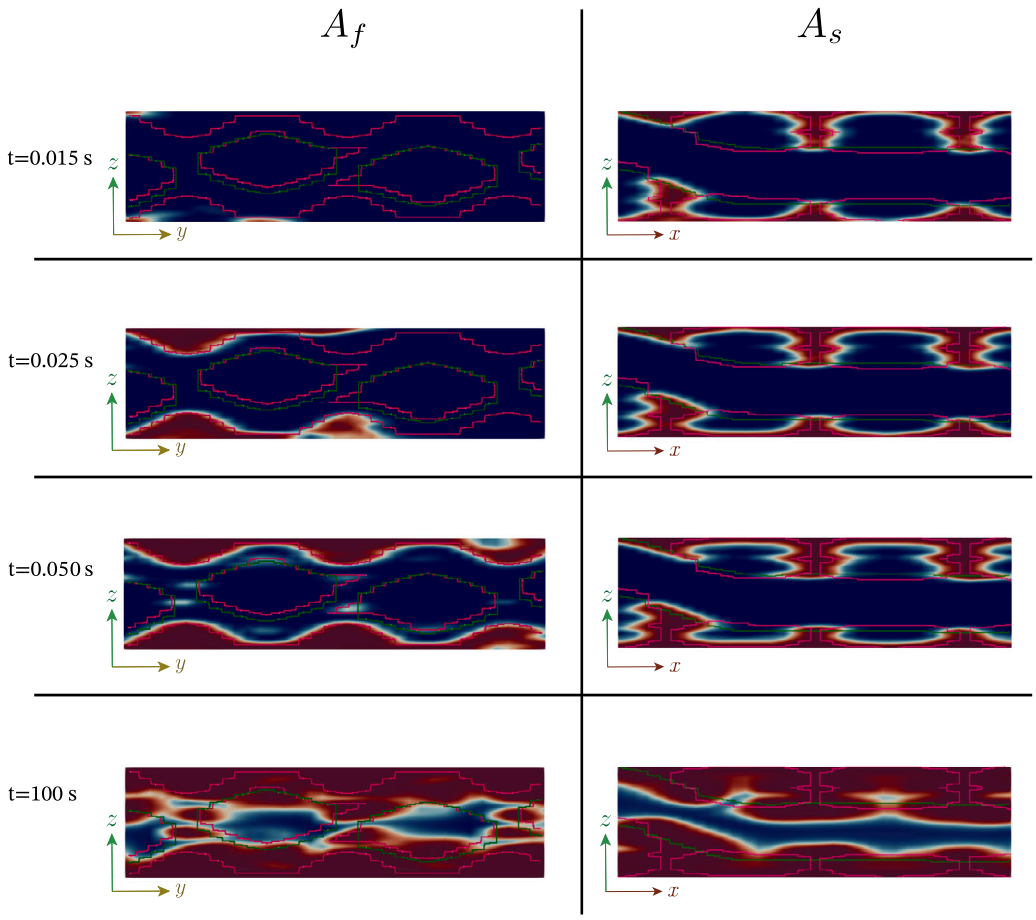

Fig. 12. Saturation of the fabric at different times along the warp direction (left column) and along the weft direction (right column) in cross sections A_f and A_s defined in Fig. 7. The color scale represents the degree of saturation, where blue color corresponds to dry areas and red areas are fully saturated. (For interpretation of the references to color in this figure legend, the reader is referred to the web version of this article.)

the tortuosity of the flow before the start of the impregnation of the fiber tows.

Figs. 15a and b show the average saturation values over time in the central volume, as well as the average pressure in the front face of the volume V_c. These results are plotted on a logarithmic scale because most of the saturation occurs in the first 0.1 s due to the rapid filling of the inter-tow gaps. The curve in Fig. 15c is obtained by combining the other two, with the values sorted from lowest to highest pressure and their corresponding saturation values.

From Fig. 15a it can be seen that the saturation of the fiber tows is a very slow process after the inter-tow gaps are filled, which is due to the very low permeability values of the fiber tows and the counter pressure of the entrapped voids within the fiber tows. What can be seen in conjunction with Fig. 15b is that the value of the pressure stabilizes at about the same time that the inter-tow gaps are filled and the fiber saturation begins. Since the pressure decreases approximately linearly between the inlet and the outlet, it stabilizes at a value close to $\Delta p/3$, since the area where the pressure is measured is at 1/3 of the distance between the two ends of the full domain.

In Fig. 15c, the unsaturated permeability curves for warp and weft flows are shown.

Following the multiphase approach, the unsaturated permeability in a given direction can be related to the saturated permeability with

$$K(S) = k_{r,l} K_{sat}, \tag{12}$$

where $k_{r,l}$ is the relative permeability relative to the liquid phase in the corresponding direction. The relative permeability is generally assumed to be a scalar quantity because saturation is generally analyzed along one direction in the frontal injection mode. However, as shown in some natural porous materials that exhibit heterogeneities and anisotropy such as fractured rocks, a tensorial form of relative permeability has been proposed [34].

If the relative permeability $\boldsymbol{k}_{r,l}$ can be considered as a tensorial quantity, then it is the ratio of the unsaturated to the saturated permeability. If the latter two are tensors, the relative permeability can be defined as

$$\boldsymbol{k}_{r,l} = \boldsymbol{K}(S) \cdot \boldsymbol{K}_{sat}^{-1} \tag{13}$$

In the case where the principal directions of unsaturated permeability are independent of saturation, the relative permeability can be defined component by component and does not need to be defined by matrix multiplication.

For the sake of simplicity, the simple form suggested in [35] is used to define the principal components of the relative permeability as a function of the saturation degree S :

$$\begin{aligned} k_{r,l}(S) &= S^2, \\ k_{r,g}(S) &= 1 - S^2. \end{aligned} \tag{14}$$

extended here in the tensorial form. $k_{r,l}$ and $k_{r,g}$ are the relative permeabilities with respect to each fluid.

For $\boldsymbol{K}_{sat}$, the components k_{warp} and k_{weft} are defined for a non-rotated fabric, in which the warp and weft directions are also the principal directions of the tensor. These values are obtained from experimental measurements (see Fig. 4) and shown in Table 5 for a volume fraction of 40%:

Going back to Fig. 15c, it can be seen that the unsaturated permeability for the warp is greater than for the weft, which is what was seen

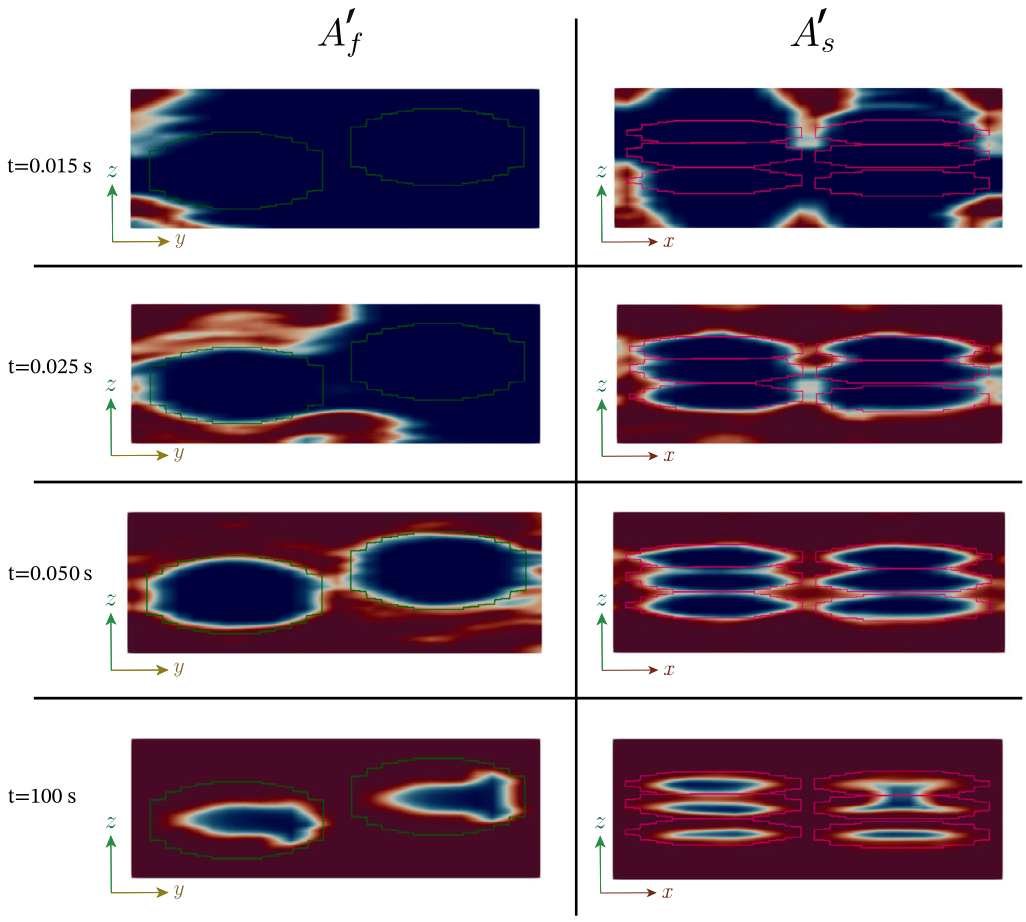

Fig. 13. Saturation of the fabric at different times along the warp direction (left column) and along the weft direction (right column) in cross sections A'_f and A'_s defined in Fig. 7. The color scale represents the degree of saturation, where blue color corresponds to dry areas and red areas are fully saturated. (For interpretation of the references to color in this figure legend, the reader is referred to the web version of this article.)

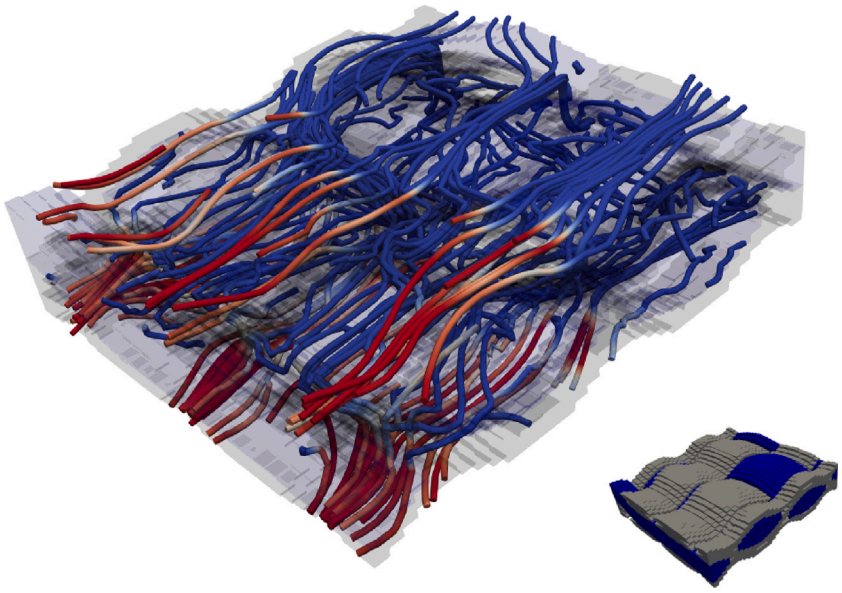

Fig. 14. Streamlines of the flow in V_C defined in Fig. 7. The color scale represents the degree of saturation, where blue color corresponds to dry areas and red areas are fully saturated. (For interpretation of the references to color in this figure legend, the reader is referred to the web version of this article.)

in the experiments. The values for the fully saturated sample are not available, but since the relative permeabilities are quadratic functions defined in Eq. (14), the values can be obtained by extrapolating the curves, as shown by the dotted lines in Fig. 15c. It has been verified that the predicted component values of $\boldsymbol{K}(S = 1)$ are equivalent to the measured values shown in Table 5.

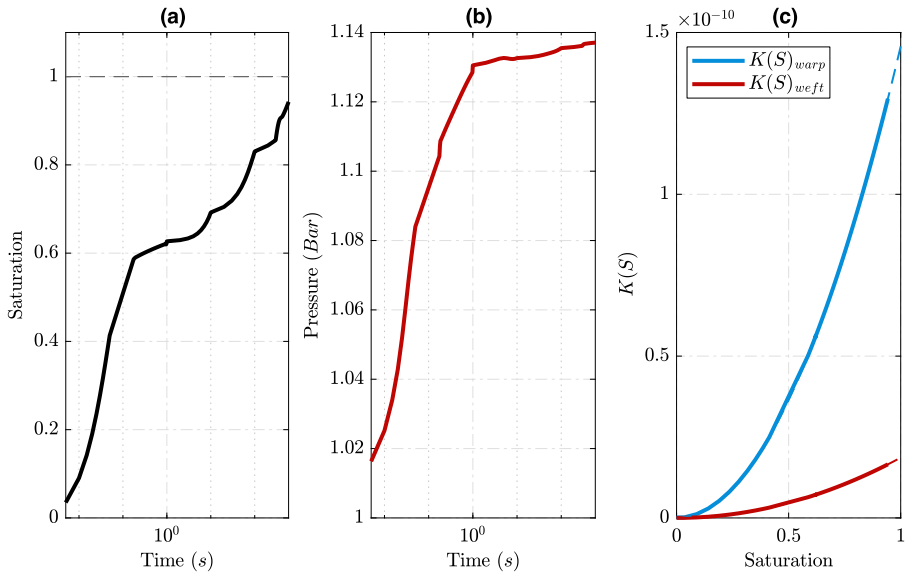

Fig. 15. Results for the simulation. (a) Saturation in central volume over time. (b) Pressure over time in central volume obtained at the upstream frontal face. (c) Unsaturated permeability $K(S)$ curves.

Table 5
Components of the saturated permeability tensor.

Component	Value
k_{warp}	$1.4572 \cdot 10^{-10}$ m^2
k_{weft}	$1.8624 \cdot 10^{-11}$ m^2

Table 6
Updated parameters for orientation analysis.

Input parameter	Value
$K_{low\ \parallel}$	$1.035 \cdot 10^{-09}$ m^2
$K_{low\ \perp}$	$2.183 \cdot 10^{-10}$ m^2

4.4. Effect of fiber orientation

To study this effect on a resin flow and whether saturation-dependent anisotropy can occur in addition to the geometric one, the simulations are performed in the same domain as before, but the fabrics are rotated. This allows to have the same boundary conditions and the same central volume, but with the fibers oriented in the prescribed angle, which should have an effect on the values of the permeability, as it was seen in the experiments.

For this analysis, the size of the elements is smaller than in the previous case. As mentioned earlier, a value must be chosen to accurately represent the geometry of the tows. Since TexGen only allows voxelized models with orientation in standard (x, y, z) axes, a rotated orientation does not provide enough resolution of the tow, which makes the solver unstable. For this reason, elements of size 0.1 mm × 0.1 mm × 0.016 mm are chosen. This means that for this mesh the number of nodes is 4,333,824 while the number of hexahedral elements is 4,250,896.

As a result of the mesh refinement, the value of the permeability in the tows is changed for these simulations to allow faster simulations than in the previous example, and to reach full saturation of the fiber tows. The values are increased by a factor of 10^4, resulting in the values shown in the Table 6.

The relevant results for this example are the saturation curves over time. Fig. 16a shows the results for all orientations. It can be seen that the saturation of the central volume occurs somewhat faster for smaller angles and slows down progressively for larger angles, which is explained by the fact that the permeability of the fabric along the warp direction is higher, allowing the resin to flow more easily. As the orientation is turned to the weft direction, the resin has more difficulty flowing and entraps air in the process, making the saturation process slower.

When calculating the unsaturated permeabilities from the saturated ones, a rotation of the form $\boldsymbol{K}'_{sat} = \boldsymbol{R}\boldsymbol{K}_{sat}\boldsymbol{R}^T$ is performed for each orientation angle θ, where $\boldsymbol{R}$ is the rotation matrix

$$\boldsymbol{R} = \begin{bmatrix} \cos\theta & -\sin\theta \\ \sin\theta & \cos\theta \end{bmatrix} \tag{15}$$

This rotated saturated permeability tensor is multiplied by the corresponding relative permeability components for each case, to obtain the unsaturated permeability for each orientation. If the unsaturated permeability is a tensorial quantity, another possible approach is to take the values for the non-rotated case and apply a rotation in a similar way to the saturated tensor. In this example, both approaches are compared. Then the quantities are calculated and plotted against each other to see if the curves are the same. If they are different, then the quantity is not tensorial.

The unsaturated permeability curves are shown in Fig. 16b. Here the phenomenon is confirmed and it can be seen that the permeability decreases as the angle of rotation increases, similar to the previous example. Also plotted here are the dashed curves representing the cases where the unsaturated permeability was rotated to the desired angles. At first glance they appear to be the same, but zooming in on the initial values of the curves shows that they are actually slightly different. Although the difference is small, it indicates that the unsaturated permeability is not necessarily a tensorial quantity for all saturation values. Although the difference is small, it indicates that the relative permeability is not perfectly aligned with the saturated permeability for all saturation values. It is believed that this slight difference may be due to the saturation dependent anisotropy direction when large voids are formed, compressed and transported. The transport of these voids, which follow tortuous paths, may deviate slightly from the principal directions of the material (warp and weft directions) as shown in the numerical simulation.

5. Conclusions

This study focused on the analysis of the directionality of the saturation of bimodal pore size distribution materials. The studied material was an anisotropic interlock with highly contrasted dual-scale porosity,

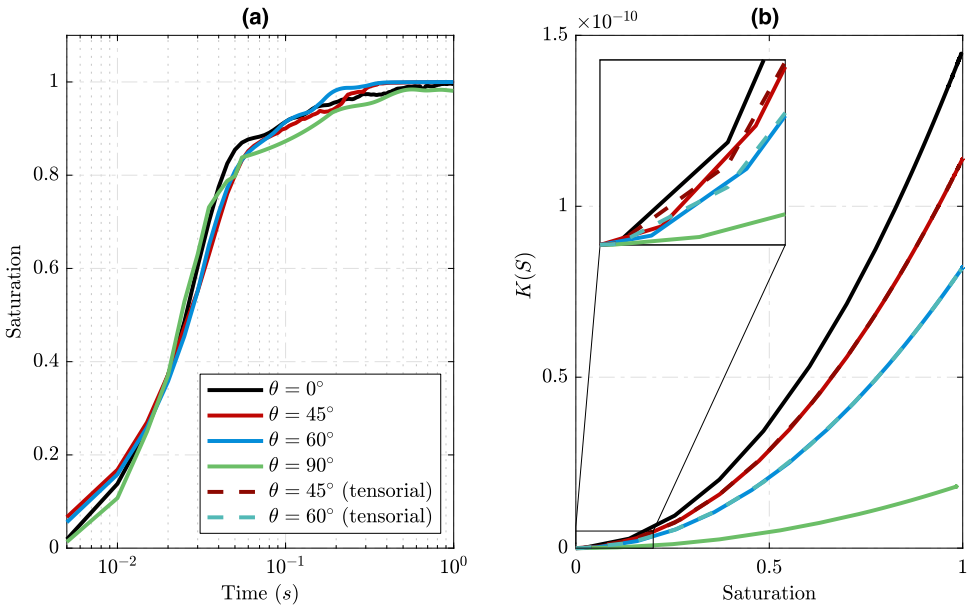

Fig. 16. (a) Saturation curves over time. (b) Unsaturated permeability $K(S)$ curves for different orientation angles.

with heavy warp and light weft tows. Experimentally, 6 configurations (3 fiber volume fraction × 2 (warp and weft) flow directions) have been tested. The experimental test consisted of injection combined with dielectric sensors in order to capture the saturation times and unsaturated lengths. The results showed that (i) this material has a high contrast in dual-scale porosity and (ii) the unsaturation is anisotropic.

The time required to ensure sufficient impregnation quality can be determined by numerical simulation, provided a model is available to accounts for the flow in porous materials with strongly bimodal pore size distributions. While this type of modeling can be done numerically at the mesoscale on a representative elementary volume, as shown in this study, this solution is not applicable to the large-scale simulation of a part. Continuum modeling is desirable, for example using a multiphase flow model. Following this approach, it has been shown that it is necessary to define a tensorial relative permeability, which has been identified in this numerical study. Simulation results suggest that, in addition to the geometric anisotropy reflected in the saturated permeability tensor, a slight saturation-dependent anisotropy can occur as a result of void transport along tortuous paths in this interlock fabric. The proposed methodology is also meant to provide a framework for experimental and computational analysis that can be applied to various textile preforms with strongly bimodal pore size distributions.

CRediT authorship contribution statement

Gabriela Gambarini: Writing – original draft, Methodology, Investigation. **Gabriel Valdés-Alonzo:** Writing – review & editing, Software, Methodology, Investigation. **Christophe Binetruy:** Writing – review & editing, Supervision, Conceptualization. **Sébastien Comas-Cardona:** Writing – original draft, Supervision, Conceptualization. **Elena Syerko:** Software, Methodology, Investigation. **Marc Waris:** Project administration, Funding acquisition.

Declaration of competing interest

The authors declare that they have no known competing financial interests or personal relationships that could have appeared to influence the work reported in this paper.

Data availability

Data will be made available on request.

References

[1] International Organization for Standardization. ISO 4410:2023 D. Test methods for the experimental characterization of in-plane permeability of fibrous reinforcements for liquid composite moulding. 2023, p. 32, ISO, Geneva, Switzerland.
[2] Bréard J, Henzel Y, Trochu F, Gauvin R. Analysis of dynamic flows through porous media. Part I: Comparison between saturated and unsaturated flows in fibrous reinforcements. Polym Compos 2003;24(3):391–408.
[3] Bancora S, Binetruy C, Advani S, Syerko E, Comas-Cardona S. Effective permeability averaging scheme to address in-plane anisotropy effects in multi-layered preforms. Composites A 2018;113:359–69.
[4] Endruweit A, Long A. Analysis of compressibility and permeability of selected 3D woven reinforcements. J Compos Mater 2010;44(24):2833–62.
[5] Alhussein H, Umer R, Rao S, Swery E, Bickerton S, Cantwell W. Characterization of 3D woven reinforcements for liquid composite molding processes. J. Mater Sci 2016;51(6):3277–88.
[6] Michaud V. A review of non-saturated resin flow in liquid composite moulding processes. Transp Porous Media 2016;115(3):581–601.
[7] Bear J, Braester C, Menier PC. Effective and relative permeabilities of anisotropic porous media. Transp Porous Media 1987;2:301–16.
[8] Adebayo AR, Barri AA, Kamal MS, et al. Effect of flow direction on relative permeability curves in water/gas reservoir system: Implications in geological CO2 sequestration. Geofluids 2017;2017.
[9] Keilegavlen E, Nordbotten JM, Stephansen AF. Tensor relative permeabilities: origins, modeling and numerical discretization. Int J Numer Anal Model 2012;9(3).
[10] LeBel F, Ruiz E, Trochu F. Experimental study of saturation by visible light transmission in dual-scale fibrous reinforcements during composite manufacturing. J Reinf Plast Compos 2017;36(23):1693–711.
[11] Nordlund M, Michaud V. Dynamic saturation curve measurement for resin flow in glass fibre reinforcement. Composites A 2012;43(3):333–43.
[12] Seto D, Matsuzaki R, Todoroki A, Mizutani Y. Void formation in an anisotropic woven fiber during resin transfer molding. In: 18th international conference on composite materials. 2011, p. 1–5.
[13] Teixidó Pedarròs H. Visualization and modelling of dynamic flow in fibrous preforms for liquid composite molding [Ph.D. thesis], Ecole Polytechnique Fédérale de Lausanne (EPFL); 2023.
[14] Labat L, Grisel M, Breard J, Bouquet G. Original use of electrical conductivity for void detection due to injection conditions of composite materials. C R Acad Sci-Ser IIB-Mechanics 2001;329(7):529–34.
[15] Laurent-Mounier A, Binétruy C, Krawczak P. Multipurpose carbon fiber sensor design for analysis and monitoring of the resin transfer molding of polymer composites. Polym Compos 2005;26(5):717–30.
[16] Carlone P, Palazzo GS. Unsaturated and saturated flow front tracking in liquid composite molding processes using dielectric sensors. Appl Compos Mater 2015;22:543–57.
[17] Carlone P, Rubino F, Paradiso V, Tucci F. Multi-scale modeling and online monitoring of resin flow through dual-scale textiles in liquid composite molding processes. Int J Adv Manuf Technol 2018;96:2215–30.

[18] Guéroult S. Analyse expérimentale de la saturation des milieux fibreux à double échelle de pores: application à la mise en oeuvre des matériaux composites par procédé RTM [Ph.D. thesis], Université du Havre; 2012.
[19] Hegg MC, Ogale A, Mescher A, Mamishev AV, Minaie B. Remote monitoring of resin transfer molding processes by distributed dielectric sensors. J Compos Mater 2005;39(17):1519–39.
[20] Pouchias A, Cunningham PR, Stein J, Kazilas M. Development of a flexible dielectric sensor for flow monitoring of the liquid resin infusion process. Sensors 2019;19(23):5292.
[21] Skordos AA, Karkanas PI, Partridge IK. A dielectric sensor for measuring flow in resin transfer moulding. Meas Sci Technol 2000;11(1):25.
[22] Tifkitsis K, Skordos AA. A novel dielectric sensor for process monitoring of carbon fibre composites manufacture. Composites A 2019;123:180–9.
[23] Yenilmez B, Sozer EM. A grid of dielectric sensors to monitor mold filling and resin cure in resin transfer molding. Composites A 2009;40(4):476–89.
[24] Weller HG, Tabor G, Jasak H, Fureby C. A tensorial approach to computational continuum mechanics using object-oriented techniques. Comput Phys 1998;12(6):620–31.
[25] Jasak H. Error analysis and estimation for the finite volume method with applications to fluid flows [Ph.D. thesis], Imperial College London; 1996.
[26] Miller S, Jasak H, Boger D, Paterson E, Nedungadi A. A pressure-based, compressible, two-phase flow finite volume method for underwater explosions. Comput & Fluids 2013;87:132–43, USNCCM Moving Boundaries.
[27] Carrillo FJ, Bourg IC, Soulaine C. Multiphase flow modeling in multiscale porous media: An open-source micro-continuum approach. J Comput Phys: X 2020;8:100073.
[28] Ivanov E, Klyuyev A, Zharkovskii A, Borshchev I. Numerical simulation of multiphase flow structures in openFOAM software package. In: E3S web of conferences, vol. 320. EDP Sciences; 2021, p. 04016.
[29] Svenungsson J. Solving electric field using maxwell's equations and compressibleInterFoam solver. 2016, CFD with OpenSource software, Chalmers University.
[30] Comas-Cardona S, Binetruy C, Krawczak P. Unidirectional compression of fibre reinforcements. Part 2: A continuous permeability tensor measurement. Compos Sci Technol 2007;67(3–4):638–45.
[31] Brown L, Long A. Modelling the geometry of textile reinforcements for composites: TexGen. In: Boisse P, editor. Composite reinforcements for optimum performance. 2nd ed.. Woodhead Publishing Ltd; 2021, p. 237–65.
[32] Gebart BR. Permeability of unidirectional reinforcements for RTM. J Compos Mater 1992;26(8):1100–33.
[33] Labat L. Etude des défauts de type vides pour la maitrise du procédé RTM [Ph.D. thesis], Université du Havre; 2001.
[34] Blonsky A, Mitrushkin D, Kudryashov I, Plynin V. Computation of absolute and relative permeability full tensors for fractured reservoirs. In: SPE Russian petroleum technology conference. SPE; 2017, D023S011R001.
[35] Gascón L, García J, LeBel F, Ruiz E, Trochu F. Numerical prediction of saturation in dual scale fibrous reinforcements during liquid composite molding. Composites A 2015;77:275–84.